Posted on 24 Nov 2022 — CC-BY-NC-ND 4 — https://doi.org/10.1002/essoar.10511575.1 — This a preprint and has not been peer reviewed. Data may be preliminary.

Long-wavelength topography and multi-scale velocity heterogeneites at the core-mantle boundary

Jack Broderick Muir[1], Satoru Tanaka[2], and Hrvoje Tkalcic[3]

[1]University of Oxford
[2]JAMSTEC
[3]Australian National University

November 24, 2022

Abstract

The structure of the lowermost mantle and the core-mantle boundary (CMB) has profound implications for Earth's evolution and current-day dynamics. Whilst tomographic studies of Vs show good agreement in the lowermost mantle, consensus as to Vp and especially CMB radius has not yet been reached. We perform a hierarchical Bayesian inversion for Vp in the lowermost 300 km of the mantle and the radius of the core-mantle boundary using differential travel time data. Concurrent with finding Vp perturbations of 0.56% RMS amplitude that spatially agree with previous studies in areas of low posterior variance, we find 4.5 km RMS amplitude core-mantle boundary radius perturbations with a broadly north-south hemispherical character, with spherical harmonic power evenly distributed between degrees 1-3. These results suggest that CMB radial processes are set by a longer scale process than the Vp perturbations.

Long-wavelength topography and multi-scale velocity heterogeneites at the core-mantle boundary

Jack B. Muir[1], Satoru Tanaka[2], Hrvoje Tkalčić[3]

[1]Department of Earth Sciences, University of Oxford,
South Parks Road, Oxford OX1 3AN, UK
[2]Volcanoes and Earth's Interior Research Center, Research Institute for Marine Geodynamics, Japan Agency for Marine-Earth Science and Technology,
2-15 Natsushima-Cho, Yokosuka 237-0061, Japan
[3]Research School of Earth Sciences, Australian National University,
142 Mills Road, Acton ACT 0200, Australia

Key Points:

- We derive a Bayesian inversion of lowermost mantle V_P structure and core-mantle boundary (CMB) topography with differential traveltime data.
- The spectra of V_P perturbations is wide, while CMB perturbations are mainly constrained to $l = 1$–3.
- These results suggest the CMB is strongly deformed by dynamic topography, and do not require a low viscosity channel in the lowermost mantle.

Corresponding author: Jack B. Muir, `jack.muir@earth.ox.ac.uk`

Abstract

The structure of the lowermost mantle and the core-mantle boundary (CMB) has profound implications for Earth's evolution and current-day dynamics. Whilst tomographic studies of V_S show good agreement in the lowermost mantle, consensus as to V_P and especially CMB radius has not yet been reached. We perform a hierarchical Bayesian inversion for V_P in the lowermost 300 km of the mantle and the radius of the core-mantle boundary using differential travel time data. Concurrent with finding V_P perturbations of 0.56% RMS amplitude that spatially agree with previous studies in areas of low posterior variance, we find 4.5 km RMS amplitude core-mantle boundary radius perturbations with a broadly north-south hemispherical character, with spherical harmonic power evenly distributed between degrees 1–3. These results suggest that CMB radial processes are set by a longer scale process than the V_P perturbations.

Plain Language Summary

The most important internal bounday of the Earth is the core-mantle boundary (CMB), between the liquid iron outer core and the rocky mantle above it. The shape of this boundary has important implications for how the Earth has evolved through time, in particular due to being an indication about how heat flows out of the core and into the mantle. However, determining this shape has remained stubbonly difficult for the past 40 years. In this paper, we use a dataset that is particularly targeted towards this region to image the CMB shape and the lowermost mantle using a robust statistical method. We find that the CMB boundary has large hills and valleys, but is relatively smooth compared to the complex structure of the lowermost mantle above it.

Introduction

The core-mantle boundary (CMB) to lowermost mantle interface is the most significant internal discontinuity of the Earth, defining an abrupt shift between the extremely viscous silicate mantle and the comparatively inviscid liquid iron-nickel alloy of the outer core. The abrupt shift in viscosity furthermore induces a thermal boundary layer in the highly heterogenous base of the mantle, presumptively with lateral variability in heat flux through the CMB contributing to mantle convection patterns. Heat flux patterns at the CMB, in turn, imprint themselves on the rapid dynamics of outer core convection and potentially on the crystallization of the inner core.

In particular, determination of CMB topography may help to distinguish the dynamical behaviour of lowermost mantle convection and lowermost mantle density Koelemeijer (2021). For example, Deschamps et al. (2018) studied the correlation between observed CMB topography, and the predicted topography from geodynamical simulations with varying viscosity and density profiles, including both static and dynamic effects. They found that CMB topography was more consistent with a thermochemical LLSVP model with high density contrast, rather than models with lower density contrasts or purely thermal models. However, due to the large discrepancies between published CMB topographic maps, explicit the characteristics of spatial correlations between LLSVP and CMB topography have not yet been determined. Multiple methodologies have been employed to attempt to resolve CMB topography (and the coupled LLSVP density problem), from body wave seismic studies (Morelli & Dziewonski (1987); Doornbos & Hilton (1989); Obayashi & Fukao (1997); Sze & van der Hilst (2003); Tanaka (2010); Schlaphorst et al. (2016)), coupled body wave / geodynamic parametrizations (Obayashi & Fukao (1997); Soldati et al. (2012, 2014)), normal mode studies (Ishii & Tromp (1999); Kuo & Romanowicz (2002); Koelemeijer et al. (2017)) and tidal tomography (Lau et al. (2017)), with typically contradictory results. There is currently little consensus as to the spatial distribution of CMB radius and density anomalies in the lowermost mantle, beyond general agreement from recent works that CMB topographic fluctuations are probably constrained to be < 10 km in peak to peak amplitude, and have generally been found to be smaller — a comprehensive review of extant seismic observations of CMB topography and related lowermost mantle density inversions is provided by Koelemeijer (2021). Consequently, further body wave tomographic studies are required to provide independent constraints on CMB topography. In particular, due to the dependence of CMB topography to the viscosity profile of the lowermost mantle (Yoshida (2008)), coupling CMB topography to lowermost mantle velocity perturbations via a geodynamical parametrization scheme (e.g. Soldati et al. (2012)) renders the resultant CMB image highly sensitive to the assumed viscosity profile of the lowermost mantle, which remains largely unknown — assuming pure isostasy (e.g. Obayashi & Fukao (1997)) is insufficient due to the significant effect of dynamic topography at long wavelengths.

Towards providing better constraints on the effect of the CMB on the dynamics of both the outer core and the mantle, our study performs a joint, spatially resolved inversion of lowermost mantle V_P perturbations and CMB radius using handpicked body wave differential travel times. The large tradeoff between CMB radius and lowermost mantle velocity perturbations suggests that a joint inversion, using data highly sensitive to CMB radius perturbations, is required to adequately discriminate between both processes (Garcia & Souriau (2000)). Indeed, in a careful study of ISC travel times, Rodgers & Wahr (1993) found that contributions from mantle heterogeneity dominated the CMB signal which were both in turn dominated by random noise; we aim to improve this situation both by using higher quality handpicked data and by performing joint inversion. Past body wave inversions have typically relied on absolute travel times for P phases. Because of the potentially significant accumulated perturbations to absolute travel times, large residuals in absolute data are not uncommon. We use three differential travel time datasets (PcP-P, PKPab-PKPbc, P4KP-PcP), carefully chosen to have complementary sensitivity for the joint inversion problem, while having restricted sensitivity to potential contamination from the upper mantle and core. In order to appropriately weight the datasets for their unknown uncertainties, we employ a hierarchical Bayesian formulation, using Hamiltonian Monte Carlo to efficiently traverse the inverse problem posterior distribution. We use a data-driven posterior predictive performance metric (PSIS-LOO) to estimate the required complexity of the inversion and appropriately truncate our model parameterization, avoiding spurious detail. The resulting inversion rigorously quantifies the uncertainties associated with this tailored dataset.

Data and Methods

We use three complementary datasets of differential body-wave travel time picks for this study. The first two datasets are the PcP-P and PKPab-PKPbc described in J. Muir & Tkalčić (2020), which in turn derive from Tkalčić et al. (2002) and Young et al. (2013) for the PcP-P data, Tkalčić et al. (2002), Leykam et al. (2010) and Young et al. (2013) for the PKPab-PKPbc data, and Tanaka (2010) for the P4KP-PcP data. All data is corrected for the Earth's ellipticity (Dziewonski & Gilbert (1976)), referenced to the ak135 1D velocity model (Kennett et al. (1995)) and further corrected for large scale mantle velocity structure using the model of Della Mora et al. (2011) to maintain consistency with Young et al. (2013) and J. Muir & Tkalčić (2020). The PcP-P dataset consists of 680 measurements with an epicentral distance of $55°$–$70°$, derived by hand-picked waveform matching of either 0.5–2 Hz bandpass filtered traces or unfiltered traces. The PcP-P dataset provides the most comprehensive coverage of the lower mantle, but is also the most affected by 3D heterogeneity of the upper mantle. The PKPab-PKPbc dataset was synthesized from finding common source/receiver pairs in a collection of PKPab-PKPdf and PKPbc-PKPdf data, resulting in 385 measurements. The original dataset was again hand-picked (by matching unfiltered waveforms with the Hilbert transform applied to the PKPab phase). The PKPdf contribution was removed to avoid contamination by the significant heterogeneity in the upper layers of the inner core. The PKPbc phase only exists in an epicentral distance range of 145°–155° and consequently the PKPab-PKPbc dataset is constrained to this range. The P4KP-PcP consists of 362 sets of differential travel time measurements, using 34 events and 242 stations. The data were selected using only unambiguous PcP and P4KP identifications, to minimize onset picking error. The distribution of the stations is predominantly concentrated in Japan, Australia and North America, and the events are concentrated in the Western Pacific and northern South America. Hence the paths of the P4KP and PcP phases in the lowermost mantle are primarily in Asia and Central America. P4KP ray paths sample the CMB in both transmission and bottomside reflection, which renders the P4KP-PcP dataset very sensitive to CMB topography. Of the various "PmKP" phases, P4KP is particularly insensitive to lowermost mantle heterogeneity when using differential travel time measurements, as its path is extremely close to the PcP ray at the same epicentral distance, as can be seen in Figure 1. High-frequency measurements of P4KP can be made due to very low, near zero, attenuation in the outer core. Consequently, P4KP-PcP is a good complementary dataset to PcP-P and PKPab-PKPbc which are more sensitive to lowermost mantle heterogeneity. Tanaka (2010) estimates a measurement error of approximately 0.5 s for this dataset, and notes that previous CMB radius inversions (Morelli & Dziewonski (1987); Doornbos & Hilton (1989); Sze & van der Hilst (2003)) do not significantly reduce the residuals of this data. The P4KP data contains waves that propagate beyond the ray-theoretical distance limit due to a tunneling effect at the CMB (Aki & Richards (2002)). These waves may be assumed to travel at the P-wave velocity of the lowermost mantle directly above the CMB (Phinney & Alexander (1966); Tanaka (2010)). The effect of topography on the travel time is included by splitting the interaction with the CMB into two parts; a contribution from the first half of the transmission at the start of the diffracted path, and then from the second half of the transmission at the end. This approximation does not take into account the topography along the path. However, this approximation is necessary to avoid recalculating the diffracted paths as topography changes, which is computationally unfeasible in the MCMC sampling context.

To study the three datasets described above, we performed a joint inversion for lowermost mantle V_P structure and CMB topography, following the study of J. Muir & Tkalčić (2020), which we summarize here, noting the adjustments performed to include the inversion for CMB radius. We modeled perturbations to the CMB radius and slowness relative to the ak135 (Kennett et al. (1995)) reference model using a spherical harmonic expansion of maximum degree l', with the optimal l' calculated as part of the inversion process. We calculated linear sensitivity kernels relating these perturbations to the differential travel times using rays drawn using the AK135 reference model by the Obspy taup module (Beyreuther et al. (2010)), which can account for the diffracted P4KP waves. We used the correction equations of Dziewonski & Gilbert (1976) to calculate kernels $\boldsymbol{G}_{\delta r}$ in respect to perturbations in CMB radius at pierce points, and integrated along the raypaths to calculate kernels $\boldsymbol{G}_{\delta s}$ in respect to perturbations in slowness. After Young et al. (2013), we perturbed slowness in the lowermost 300 km of the mantle only, and assumed that slownesses were radially constant within that depth range. The reference velocity for these perturbations is the radial average over the lowermost 300 km, which gives 13.61 km/s. For computing the effect of radius perturbations, we used a velocity of 13.66 km/s above the CMB and 8.0 km/s below the CMB, and a reference radius of 3479.5 km. While anisotropy is an important consideration for a full description of the lowermost mantle, the effect on P-wave energy is likely dominated by short scale structures associated with flow gradients (e.g. Garnero et al. (2004)), that will be smoothed by the long-wavelength tomography we investigate in this study; therefore we do not include the effect of anisotropy in our forward predictions.

The forward model prediction $\Delta\boldsymbol{t}^*(\boldsymbol{q}_{\delta r}, \boldsymbol{q}_{\delta s})$ for the inversion for the collected differential travel time data $\Delta\boldsymbol{t}$ is then

$$\Delta\boldsymbol{t}^*(\boldsymbol{q}_{\delta r}, \boldsymbol{q}_{\delta s}) = \begin{bmatrix} \boldsymbol{G}_{\delta r} \\ \boldsymbol{G}_{\delta s} \end{bmatrix}^T \begin{bmatrix} \boldsymbol{q}_{\delta r} \\ \boldsymbol{q}_{\delta s} \end{bmatrix}, \tag{1}$$

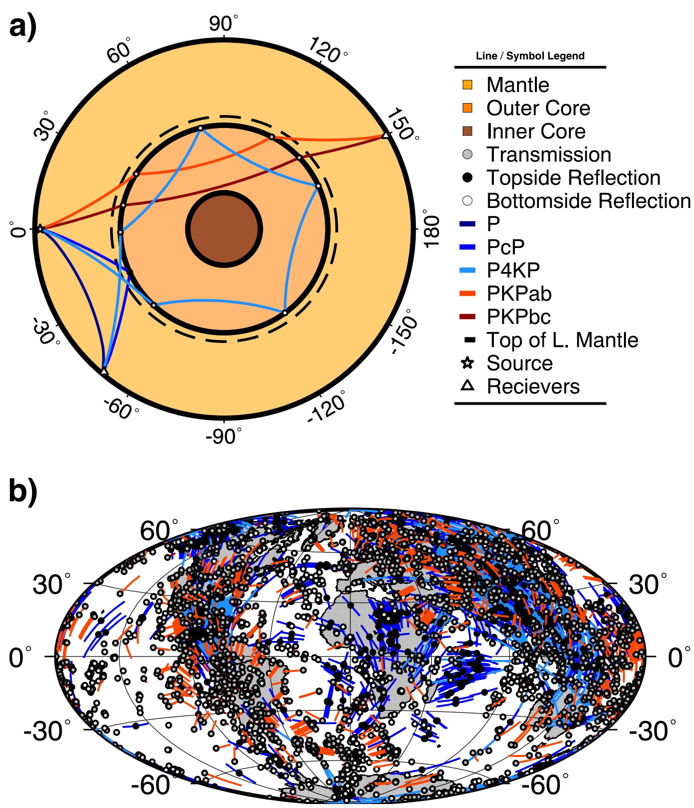

Figure 1. Summary of data used in this study. a) shows characteristic ray paths through the lowermost mantle, and their CMB pierce points. b) shows the map projection of these paths and pierce points in the lowermost 300 km of the mantle. HALF PAGE WIDTH

for spherical harmonic expansion coefficients of CMB radius $\boldsymbol{q}_{\delta r}$ and lowermost mantle slowness $\boldsymbol{q}_{\delta s}$. The PcP-P dataset contributes heavily to the V_P sensitivity and relatively little to CMB radius sensitivity; P4KP-PcP is the opposite, while PKPab-PKPbc contributes moderately to sensitivity to both components and also adds additional sensitivity to odd-degree CMB radius structure. Of note are the large number of similar PKPab-PKPbc rays that form a subset with nearly the same sensitivity, and the relative lack of sensitivity of P4KP-PcP to odd-degree CMB structure. Recent work on finite-frequency kernel calculations for CMB sensitive phases (e.g. Koroni et al. (2021)) have also stressed the relative lack of sensitivity of "traditional" phases (PKP, PcP) to CMB structure compared to their sensitivity to volumetric lowermost mantle velocity perturbations, highlighting the importance of tailoring the dataset to the CMB through the inclusion of P4KP. The relative sensitivity of the three datasets to V_P and CMB radius is shown in Supplementary Figure S1.

We use a hierarchical Bayesian modeling framework to account for the unknown data uncertainties σ_{PcP-P}, $\sigma_{PKPab-PKPbc}$ and $\sigma_{P4KP-PcP}$, and *a priori* unknown scales $\sigma_{\delta r}$ and $\sigma_{\delta s}$ of $\boldsymbol{q}_{\delta r}$ and $\boldsymbol{q}_{\delta s}$ respectively. These five unknown scales $\boldsymbol{\sigma}$ act as hyperparameters for the inversion, and are simultaenously with the main parameters. The posterior probability distribution is calculated via Bayes' theorem as the product of data likelihood, prior distribution and hyperprior distribution:

$$P(\boldsymbol{q}_{\delta r}, \boldsymbol{q}_{\delta s}, \boldsymbol{\sigma}|\Delta \boldsymbol{t}) = P(\Delta \boldsymbol{t}|\boldsymbol{q}_{\delta r}, \boldsymbol{q}_{\delta s}, \boldsymbol{\sigma})P(\boldsymbol{q}_{\delta r}, \boldsymbol{q}_{\delta s}|\boldsymbol{\sigma})P(\boldsymbol{\sigma}). \tag{2}$$

This hierarchical modeling framework makes the inversion non-linear despite the linear foward model, but has the advantage of marginalizing over unknown errors when the posterior statistics are calculated. The data are assumed to follow a Gaussian distribution, so that the data likelihood for e.g. the PcP-P dataset is calculated by multiplying the likelihood for each datum as follows:

$$P(\Delta \boldsymbol{t}_{PcP-P}|\boldsymbol{q}_{\delta r}, \boldsymbol{q}_{\delta s}, \sigma_{PcP-P}) = \prod_{i=1}^{\#PcP-P} \frac{1}{\sqrt{2\pi\sigma^2_{PcP-P}}} \exp\left[-\frac{(\Delta \boldsymbol{t}_{PcP-P} - \Delta \boldsymbol{t}^*_{PcP-P}(\boldsymbol{q}_{\delta r}, \boldsymbol{q}_{\delta s}))_i^2}{2\sigma^2_{PcP-P}}\right]. \tag{3}$$

Given that we are inverting for perturbations about a well established reference model, we set the prior distributions for $\boldsymbol{q}_{\delta r}$ and $\boldsymbol{q}_{\delta s}$ to be normal distributions with zero mean and standard deviations of $\sigma_{\delta r}$ and $\sigma_{\delta s}$, respectively. Following J. Muir & Tkalčić (2020), we use half-normal distributions with wide standard-deviations for the hyperprior distrubutions. The hyperprior for e.g. $\sigma_{\delta r}$ is given by

$$P(\sigma_{\delta r}) = \frac{\sqrt{2}}{\sqrt{\pi^2\nu^2_{\delta r}}} \exp\left[-\frac{\sigma^2_{\delta r}}{2\nu^2_{\delta r}}\right], \qquad \sigma_{\delta r} > 0, \tag{4}$$

with the five ν set to the values in Supplementary Table S1. The total posterior distribution is given by multiplying the three data likelihoods, two priors and five hyperpriors together. The total number of parameters is therefore $2(2l' + 1) + 5$. Due to the aforementioned non-linearity of the posterior, we characterise the parameters by using Markov-Chain Monte-Carlo (MCMC) methods to sample from the posterior distribution. Expectation values (e.g. the posterior mean perturbations velocity and CMB radius) are easily computed from MCMC chains, and automatically marginalize over the unknown hyperparameters. MCMC sampling is computationally expensive, and for this problem the number total parameters could be in excess of 100, which is infeasible for classical MCMC methods such as the Metropolis-Hastings method. In order to efficiently sample, we used Hamiltonian Monte-Carlo (HMC), which uses gradient information in the posterior to improve the rate of mixing of the MCMC chains (Neal (2011); M. Betancourt et al. (2017)). The efficiency of HMC in sampling large, weakly nonlinear problems make it eminently suitable for many geophysical problems (e.g. Sen & Biswas (2017); Biswas & Sen (2017); Fichtner & Simutė (2018); Fichtner et al. (2019); J. Muir & Tkalčić (2020); Fichtner et al. (2021)). In this study, we used the STAN (Carpenter et al. (2017))

language to define the model and automatically compute the posterior gradients. The efficiency of sampling is further improved by transforming the parameters into a non-centered coordinate system (M. J. Betancourt & Girolami (2013)), by defining $\boldsymbol{q}_{\delta r} = \sigma_{\delta r}\boldsymbol{q}'_{\delta r}$ and $\boldsymbol{q}_{\delta s} = \sigma_{\delta s}\boldsymbol{q}'_{\delta s}$. The prior distribution for the auxiliary variables $\boldsymbol{q}'_{\delta r}$ and $\boldsymbol{q}'_{\delta s}$ are standard normal distributions with zero mean and unit standard deviation. This coordinate transform avoids the "funnel" effect (Neal (2003)) that is a common pathology for hierarchical Bayesian models with relatively large data uncertainty. To check that MCMC chains are appropriately sampling, we used a variety of diagnostics as suggested by the STAN team, including confirming inter-chain consistency with the $\hat{R}$ metric, ensuring a lack of divergences during sampling etc. (Gelman et al. (2013)).

In order to appropriately match the complexity of the model parametization to the data, we performed the inversion for expansions of maximum degree $l' = 0$–15. As in J. Muir & Tkalčić (2020), we use the PSIS-LOO estimator (Vehtari et al. (2017)) of the leave-one-out cross-validation (LOO-CV) score for each degree to assess model complexity. The LOO-CV score for a collection of data $\boldsymbol{d}$ is given by

$$\text{LOO-CV}(\boldsymbol{d}) = \sum_i \log P(\boldsymbol{d}_i|\boldsymbol{d}_{j\neq i}) \tag{5}$$

where the posterior predictive for the left-out data $\boldsymbol{d}_i$ is given by

$$P(\boldsymbol{d}_i|\boldsymbol{d}_{j\neq i}) = \int P(\boldsymbol{d}_i|\boldsymbol{q})P(q|\boldsymbol{d}_{j\neq i})d\boldsymbol{q}. \tag{6}$$

Explicit computation of LOO-CV is expensive, as it requires marginalization (i.e. a full MCMC run) over model parameters for each data point to compute the integral in Equation 6; the PSIS-LOO estimator gives accurate results for the great majority of data points using a single MCMC run. The remaining data points for which PSIS-LOO fails may be identified and sampled normally, overall resulting in a substantial computational saving (Vehtari et al. (2017)). We apply Occam's razor to the LOO-CV results, taking the lowest l' for which no higher tested l' give a better result within a 2 standard deviation uncertainty in LOO-CV predicted performance.

Results and Discussion

We first investigate the estimated LOO-CV curve for different maximum degrees l' to set the expansion degree for the rest of the analysis. Figure 2 shows the estimated LOO-CV score, relative to a maximum degree $l' = 8$. Error bars in the difference of the score are given at the 2 standard deviation level. We see that the score rapidly improves up to $l' = 8$, and then saturates for higher degrees, with no statistically significant improvement of the score on adding more parameters to the inversion. As such, the remainder of this study takes $l' = 8$ as the highest degree of expansion for both CMB and lowermost mantle inversion that can be supported by the data. We note that it is possible to perform the expansion at different maximum degrees for the lowermost mantle and CMB radius inversions, however this complicates comparison between the components of the model and so we do not investigate it here. A similar alternative methodology would be to marginalize over the maximum expansion degree using automatic relevance determination (ARD), which uses additional hyperparameters to dynamically remove complexity from within the MCMC chain (Valentine & Sambridge (2018)). However given the rapid saturation of performance $l' = 8$ appears not to warrant the additional computational expense of ARD in this case.

The resulting V_P model (in Figure 3, with residual histograms in Supplementary Figure S2) is strongly similar to J. Muir & Tkalčić (2020), which is an inversion of the lowermost-mantle only and does not include the P4KP-PcP dataset but otherwise uses the same methodology. Consequently, the model is also similar to Young et al. (2013), from which the PcP and PKPab-PKPbc datasets were derived, although Young et al.

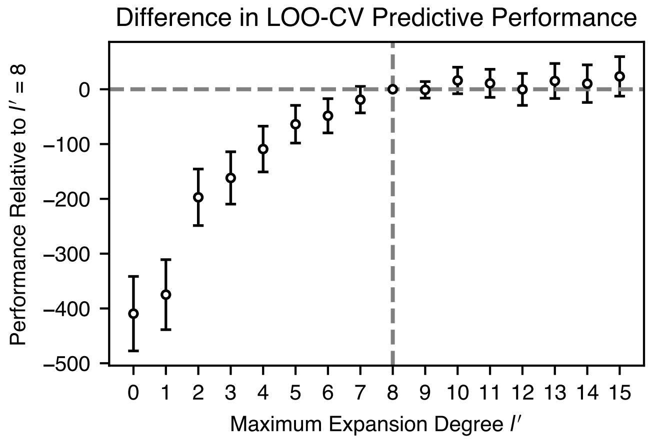

Figure 2. Relative LOO-CV performance for degrees $l' = 0$–15. LOO-CV scores are given relative to $l' = 8$, with error bars showing the uncertainty in the difference at a 2 standard deviation level. HALF PAGE WIDTH

(2013) used a transdimensional Bayesian approach and inverted PKPab and PKPbc data relative to the PKPdf phase, which also samples the highly heterogenous outer layers of the inner core. The V_P RMS perturbation is 0.56%, which is smaller than the 0.71% reported in J. Muir & Tkalčić (2020) and the 0.87% reported in Young et al. (2013), potentially as the residuals in previous inversions contained unmodelled contributions from the CMB topography (and inner core for Young et al. (2013)), but also potentially due to smoothing induced by truncation of the model to a lower degree. That spatial distribution of velocity perturbations is very similar between the three models suggests that the errors induced by not taking into account CMB perturbations did not significantly impact the conclusions drawn by the two previous studies using these data for Bayesian inversion. As earlier discussed in J. Muir & Tkalčić (2020), this spatial pattern is dominated by a large fast patch underneath Asia, and broad areas of low velocity that correspond with the locations of the large low velocity provinces albeit with greater connectivity, as suggested by the model of Hosseini et al. (2020). The fast velocities under the east Pacific in this model are in the region of the highest model uncertainty due to a lack of ray coverage, and are not in disagreement with the general shape of the Pacific LLVP at a statistically significant level. Following J. Muir & Tkalčić (2020), the most interesting outcome of this V_P inversion is that when this diverse collection of short-period differential travel times is used for lowermost mantle V_P inversion, the resulting power spectrum is relatively flat rather than being red — degree 2 power is the strongest but is not dominant — which tends to support a view of a thermally driven lowermost mantle with multiscale structure (Tkalčić et al. (2015)). The large degree 0 component is likely due to the ray-average velocity being different to the vertical-average velocity in the lowermost 300 km of the mantle.

Contrary to the distribution of V_P perturbations, our inversion for CMB radius, shown in Figure 3 shows a map dominated by power distributed between degrees 1-3, again with a large degree 0 component that can be regarded as a static correction as the CMB mean radius is not constrained. The RMS CMB perturbation is 4.5 km, and the pattern has strong qualitative resemblance to Tanaka (2010), although with significantly increased amplitude. Given that we believe degree 8 is potentially resolvable given our data, this suggests that the inversion in Tanaka (2010) is oversmoothed due to basis truncation. Figure 4 shows the correlation structure between velocity and CMB radius per-

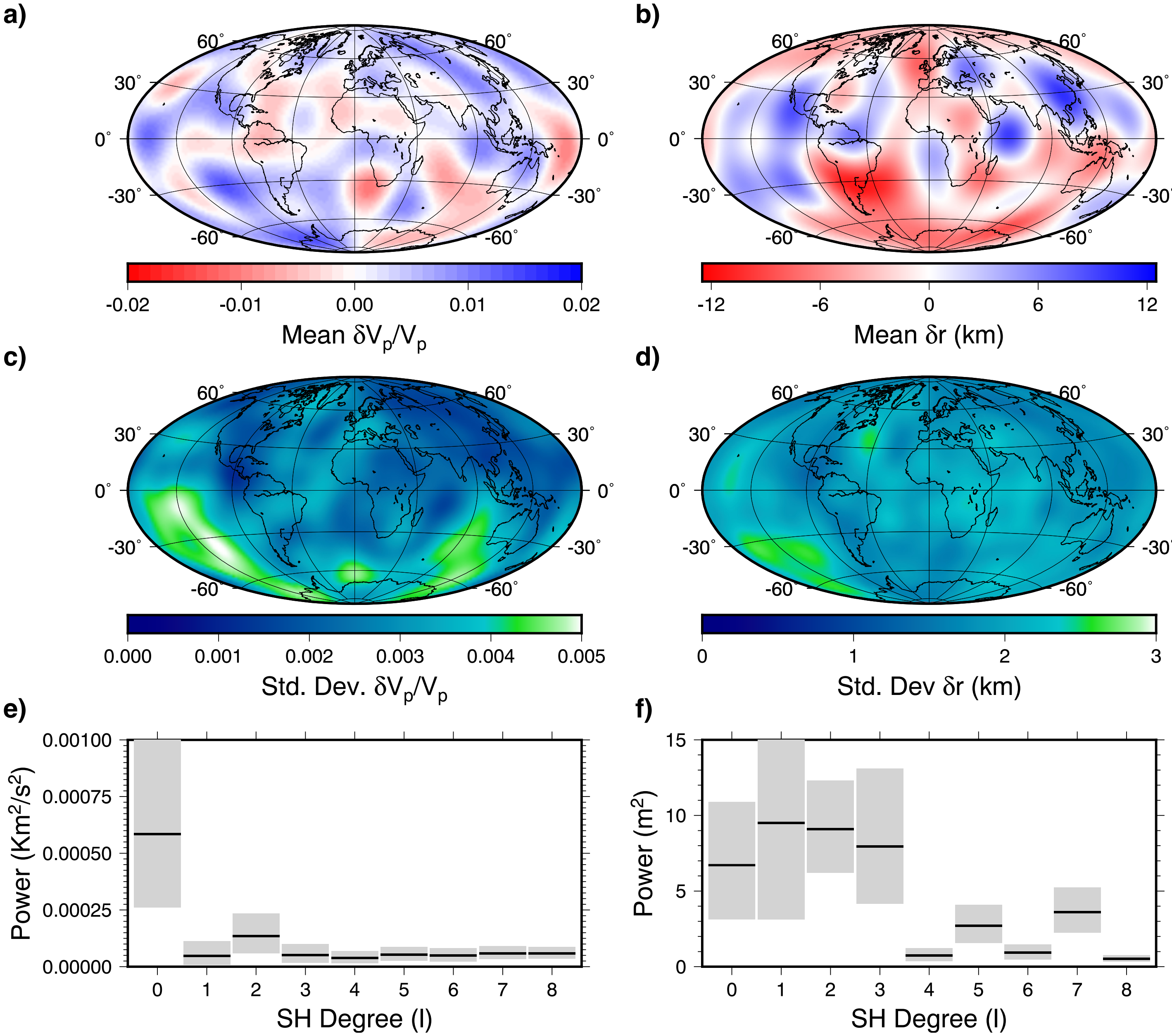

Figure 3. Summary of the outcomes of the inversion; a) shows the mean percentage perturbation in V_P, c) shows the standard deviation of the MCMC chain for percentage perturbation of V_P, and e) shows the power spectrum as a function of l. All assume a reference velocity of 13.61 km/s. b), d) and f) show the equivalent for the perturbation in CMB radius. All assume a reference CMB radius of 3479.5 km. FULL PAGE WIDTH

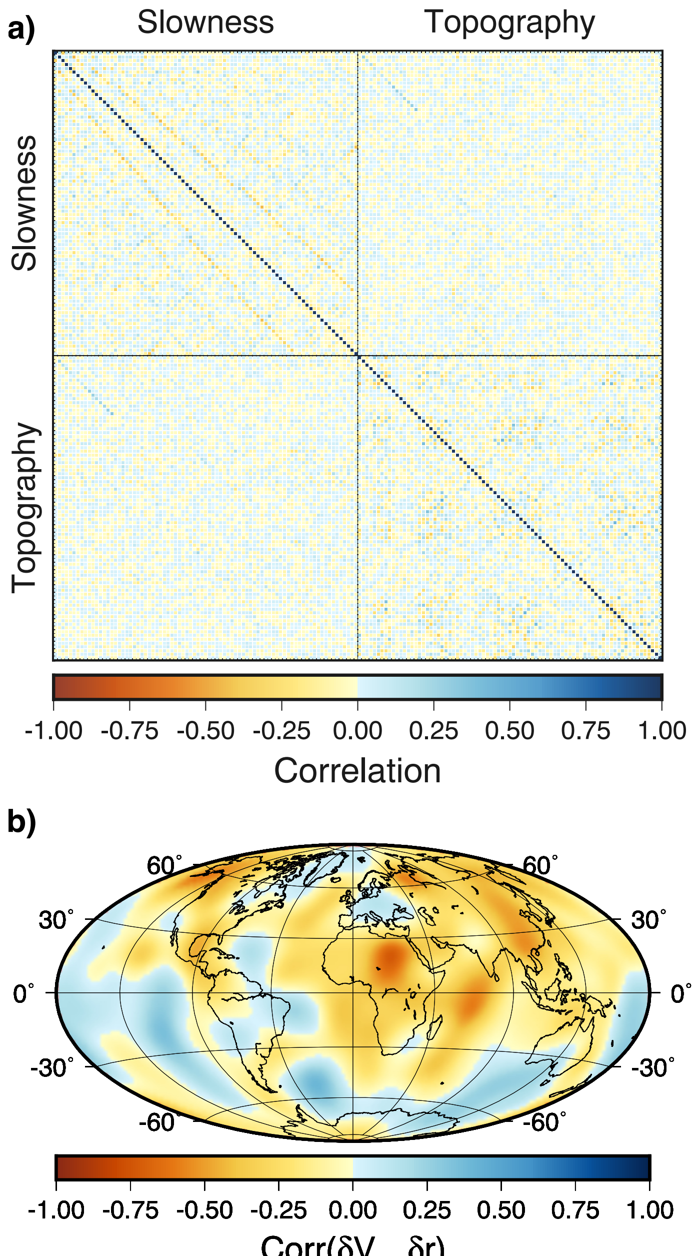

Figure 4. Correlations between CMB radius and lowermost mantle velocity. a) shows the correlation between P slowness perturbations and topographic perturbations per degree in the MCMC chain. b) shows the spatial correlation between V_P and radius after the spherical harmonic components are summed. The reference V_P is 13.61 km/s and the reference CMB radius is 3479.5 km. HALF PAGE WIDTH

turbations, as a function of both model parameter and spatial location. In both cases, we see that the correlation is relatively small in both cases, indicating that both velocity and radius perturbations do not strongly trade off. The exceptions (in well resolved areas), seen in Figure 4 b) occur primarily underneath northern Africa and Asia where there is a significant negative correlation between velocity perturbations and CMB radius. For PcP-P data, higher lowermost mantle velocities can be compensated by a lower CMB radius to maintain a constant travel time along a PcP phase. The effect is the opposite for P4KP, for which a lower CMB produces a faster travel time, so areas with many rays of both PcP-P and P4KP-PcP should have better constraints on the tradeoff between CMB radius and Vp perturbations. The strong African negative correlation can then be explained the presence of PcP-P and lack of P4KP-PcP rays. The weaker negative correlations in Asia, where P4KP is present, may be indicative of the PcP data having a stronger control on the posterior than P4KP; note that the posterior standard deviations in Asia are some of the lowest in the inversion, so despite the negative correlation the absolute size of the tradeoff is relatively small. The strong positive velocity anomaly underneath Asia is accompanied by a large positive CMB perturbation, despite the negative correlation. There is as yet little concordance between maps of CMB topography inverted from seismic travel times, despite increasing coupled treatment of lowermost mantle heterogeneity. This observation remains true whether relying purely on seismic data (Morelli & Dziewonski (1987); Doornbos & Hilton (1989); Sze & van der Hilst (2003); Tanaka (2010)) or geodynamically coupled tomography (Soldati et al. (2012, 2014)). This study complements previous work by performing the inversion with only the highest quality available data, and using an inversion technique that gives us a fuller picture of the remaining tradeoffs and uncertainties in the lowermost mantle and CMB.

The low degree structure of the CMB perturbations, in contrast to the spatially broadband power spectrum of V_P perturbations, suggests that its structure is set by longer wavelength processes. The lack of correlation between V_P and CMB radius spatial variations also strongly suggests that the impact of isostasy on the CMB is minimal (assuming scaling between density and V_P perturbations), and that instead dynamic topography is the primary contributor to the CMB radius. The amplitude of dynamic topography due to instantaenous mantle flow scales with viscosity and the gradient of vertical flow velocity. Yoshida (2008) required either reductions of mantle viscosity compared to a $10^{21} Pa$ reference, or lateral viscosity variations, to suppress CMB amplitudes to match the low values found by Sze & van der Hilst (2003). Our results permit a significantly larger range of CMB radial perturbations and so do not infer a significant depression in lowermost mantle viscosity near the CMB. From the perspective of the outer core, Calkins et al. (2012) showed that negative CMB topography may induce strong, persistent flow features within the outer core convection, scaling with topographic amplitude. This topographic effect significantly increases the vigour of outer core convection and hence the rate of heat flow, providing an additional (potentially coupled) top-down control on outer core convection beyond laterally varying heat flux due to mantle heterogeneity, and in turn further contributes downward pressure on estimates of inner core nucleation age (Olson (2016)). Tarduno et al. (2015) invoked flux expulsion from small-scale flow structures associated with a high-topographic gradient isostatic African LLSVP to explain the historical persistence of the South Atlantic geomagnetic Anomaly (SAA) — intriguingly, the largest negative topographic anomaly in our model is also coincident with the SAA, and the long wavelength topographic flow effects studied by Calkins et al. (2012) acting on this feature may present an alternative stabilizing mechanism for persistent geomagnetic anomalies in this region even if the African LLSVP is uplifted by dynamic topography.

As noted by Lassak et al. (2007, 2010), the morphology of the CMB depends on a complex mix of density, temperature and viscosity profiles. Our model, whilst expanded to a higher degree than previous CMB profiles, does not permit the falsification of the various end members of potential CMB morphology without further constraints on at least some of these parameters. Further development of the joint tomography presented in this work will require greater density of data coverage, especially CMB radius sensitive phases such as P4KP that require careful processing in excess of that provisioned by catalogue data (Tanaka (2010); Schlaphorst et al. (2016)).

Conclusions

We have obtained the lowermost mantle structure along with the radial perturbations of the CMB, finding that lowermost mantle velocity structure is highly multiscale, while the CMB radial perturbations are dominated by $l < 3$. Velocity amplitude perturbations with RMS 0.56% are in line with previous estimates of lowermost mantle heterogeneity, while CMB radial perturbations of 4.5 km are relatively large by the standards of recent inversions, which may be ascribed to the data-driven regularization of the problem and appropriate joint treatment of lowermost mantle heterogeneity. These long wavelength CMB structures present a complementary top-down driven control on outer core convection, in addition to lateral heat-flux variability due to structural heterogeneity in the lowermost mantle, and suggest a CMB landscape dominated by dynamic topography due to mantle overturning, without a low-viscosity channel in the lowermost mantle. Further studies of CMB topographic anomalies and their relationship to lowermost mantle structure are contingent on development of larger high-sensitivity datasets for this region, and in particular more comprehensive observations of the elusive family of PmKP waves that have strong sensitivity to the CMB radius.

Model Availability

The model is available on Zenodo as J. B. Muir et al. (2022a) at the following URL: `https://zenodo.org/record/6525050`. The data and code used for generating the model are also on Zenodo as J. B. Muir et al. (2022b) at the following URL: `https://zenodo.org/record/6619144`.

Acknowledgements

JBM acknowledges the support of the John Monash and Origin Energy foundations during his PhD studies.

References

Aki, K., & Richards, P. G. (2002). *Quantitative seismology.* University Science Books.

Betancourt, M., Byrne, S., Livingstone, S., & Girolami, M. (2017, November). The geometric foundations of Hamiltonian Monte Carlo. *Bernoulli*, *23*(4A), 2257–2298. doi: 10.3150/16-BEJ810

Betancourt, M. J., & Girolami, M. (2013, December). Hamiltonian Monte Carlo for Hierarchical Models. *arXiv:1312.0906 [stat]*.

Beyreuther, M., Barsch, R., Krischer, L., Megies, T., Behr, Y., & Wassermann, J. (2010, May). ObsPy: A Python Toolbox for Seismology. *Seismological Research Letters*, *81*(3), 530–533. doi: 10.1785/gssrl.81.3.530

Biswas, R., & Sen, M. (2017). 2D Full-Waveform Inversion and Uncertainty Estimation using the Reversible Jump Hamiltonian Monte Carlo. In *SEG Technical Program Expanded Abstracts 2017* (pp. 1280–1285). Society of Exploration Geophysicists.

Calkins, M. A., Noir, J., Eldredge, J. D., & Aurnou, J. M. (2012, May). The effects of boundary topography on convection in Earth's core. *Geophysical Journal International*, *189*(2), 799–814. doi: 10.1111/j.1365-246X.2012.05415.x

Carpenter, B., Gelman, A., Hoffman, M. D., Lee, D., Goodrich, B., Betancourt, M., ... Riddell, A. (2017). Stan: A probabilistic programming language. *Journal of statistical software*, *76*(1).

Della Mora, S., Boschi, L., Tackley, P. J., Nakagawa, T., & Giardini, D. (2011, June). Low seismic resolution cannot explain S/P decorrelation in the lower mantle. *Geophysical Research Letters*, *38*(12), n/a-n/a. doi: 10.1029/2011GL047559

Deschamps, F., Rogister, Y., & Tackley, P. J. (2018, January). Constraints on core–mantle boundary topography from models of thermal and thermochemical convection. *Geophysical Journal International*, *212*(1), 164–188. doi: 10.1093/gji/ggx402

Doornbos, D. J., & Hilton, T. (1989, November). Models of the core-mantle boundary and the travel times of internally reflected core phases. *Journal of Geophysical Research: Solid Earth*, *94*(B11), 15741–15751. doi: 10.1029/JB094iB11p15741

Dziewonski, A. M., & Gilbert, F. (1976). The effect of small, aspherical perturbations on travel times and a re-examination of the corrections for ellipticity. *Geophysical Journal of the Royal Astronomical Society*, *44*(1), 7–17.

Fichtner, A., & Simutė, S. (2018, April). Hamiltonian Monte Carlo Inversion of Seismic Sources in Complex Media. *Journal of Geophysical Research: Solid Earth*, *123*(4), 2984–2999. doi: 10.1002/2017JB015249

Fichtner, A., Zunino, A., & Gebraad, L. (2019, February). Hamiltonian Monte Carlo solution of tomographic inverse problems. *Geophysical Journal International*, *216*(2), 1344–1363. doi: 10.1093/gji/ggy496

Fichtner, A., Zunino, A., Gebraad, L., & Boehm, C. (2021, July). Autotuning Hamiltonian Monte Carlo for efficient generalized nullspace exploration. *Geophysical Journal International*, *227*(2), 941–968. doi: 10.1093/gji/ggab270

Garcia, R., & Souriau, A. (2000, January). Amplitude of the core–mantle boundary topography estimated by stochastic analysis of core phases. *Physics of the Earth and Planetary Interiors*, *117*(1-4), 345–359. doi: 10.1016/S0031-9201(99)00106-5

Garnero, E. J., Maupin, V., Lay, T., & Fouch, M. J. (2004, October). Variable Azimuthal Anisotropy in Earth's Lowermost Mantle. *Science*, *306*(5694), 259–261. doi: 10.1126/science.1103411

Gelman, A., Stern, H. S., Carlin, J. B., Dunson, D. B., Vehtari, A., & Rubin, D. B. (2013). *Bayesian data analysis*. Chapman and Hall/CRC.

Hosseini, K., Sigloch, K., Tsekhmistrenko, M., Zaheri, A., Nissen-Meyer, T., & Igel, H. (2020, January). Global mantle structure from multifrequency tomography using P, PP and P-diffracted waves. *Geophysical Journal International*, *220*(1), 96–141. doi: 10.1093/gji/ggz394

Ishii, M., & Tromp, J. (1999). Normal-mode and free-air gravity constraints on lateral variations in velocity and density of Earth's mantle. *Science*, *285*(5431), 1231–1236.

Kennett, B. L. N., Engdahl, E. R., & Buland, R. (1995, July). Constraints on seismic velocities in the Earth from traveltimes. *Geophysical Journal International*, *122*(1), 108–124. doi: 10.1111/j.1365-246X.1995.tb03540.x

Koelemeijer, P. (2021). Toward Consistent Seismological Models of the Core–Mantle Boundary Landscape. In *Mantle Convection and Surface Expressions* (pp. 229–255). Wiley Online Library.

Koelemeijer, P., Deuss, A., & Ritsema, J. (2017, May). Density structure of Earth's lowermost mantle from Stoneley mode splitting observations. *Nature Communications*, *8*, 15241. doi: 10.1038/ncomms15241

Koroni, M., Borgeaud, A., Fichtner, A., & Deschamps, F. (2021, October). Analysis of core-mantle boundary seismic waves using full\-waveform modelling and adjoint methods. *arXiv:2110.11068 [physics]*.

Kuo, C., & Romanowicz, B. (2002, July). On the resolution of density anomalies in the Earth's mantle using spectral fitting of normal-mode data. *Geophysical Jour-*

nal International, *150*(1), 162–179. doi: 10.1046/j.1365-246X.2002.01698.x

Lassak, T. M., McNamara, A. K., Garnero, E. J., & Zhong, S. (2010, January). Core–mantle boundary topography as a possible constraint on lower mantle chemistry and dynamics. *Earth and Planetary Science Letters*, *289*(1-2), 232–241. doi: 10.1016/j.epsl.2009.11.012

Lassak, T. M., McNamara, A. K., & Zhong, S. (2007, September). Influence of thermochemical piles on topography at Earth's core–mantle boundary. *Earth and Planetary Science Letters*, *261*(3-4), 443–455. doi: 10.1016/j.epsl.2007.07.015

Lau, H. C. P., Mitrovica, J. X., Davis, J. L., Tromp, J., Yang, H.-Y., & Al-Attar, D. (2017, November). Tidal tomography constrains Earth's deep-mantle buoyancy. *Nature*, *551*(7680), 321–326. doi: 10.1038/nature24452

Leykam, D., Tkalčić, H., & Reading, A. M. (2010, March). Core structure reexamined using new teleseismic data recorded in Antarctica: Evidence for, at most, weak cylindrical seismic anisotropy in the inner core. *Geophysical Journal International*, *180*(3), 1329–1343. doi: 10.1111/j.1365-246X.2010.04488.x

Morelli, A., & Dziewonski, A. M. (1987, February). Topography of the core–mantle boundary and lateral homogeneity of the liquid core. *Nature*, *325*(6106), 678–683. doi: 10.1038/325678a0

Muir, J., & Tkalčić, H. (2020, September). Probabilistic lowermost mantle P-wave tomography from hierarchical Hamiltonian Monte Carlo and model parametrization cross-validation. *Geophysical Journal International*, *223*(3), 1630–1643. doi: 10.1093/gji/ggaa397

Muir, J. B., Tanaka, S., & Tkalčić, H. (2022a, May). *CMB / Lowermost Mantle Joint Tomographic Model.* Zenodo. doi: 10.5281/zenodo.6525050

Muir, J. B., Tanaka, S., & Tkalčić, H. (2022b, June). *Data & parsing software for CMB Topographic Model.* Zenodo. doi: 10.5281/zenodo.6619144

Neal, R. M. (2003). Slice sampling. *Annals of statistics*, 705–741.

Neal, R. M. (2011). MCMC using Hamiltonian dynamics. *Handbook of Markov Chain Monte Carlo*, *2*(11).

Obayashi, M., & Fukao, Y. (1997, August). P and PcP travel time tomography for the core-mantle boundary. *Journal of Geophysical Research: Solid Earth*, *102*(B8), 17825–17841. doi: 10.1029/97JB00397

Olson, P. (2016). Mantle control of the geodynamo: Consequences of top-down regulation. *Geochemistry, Geophysics, Geosystems*, *17*(5), 1935–1956. doi: 10.1002/2016GC006334

Phinney, R. A., & Alexander, S. S. (1966). P Wave Diffraction Theory and the Structure of the Core-Mantle Boundary. *Journal of Geophysical Research*, *71*(24), 5959–5975.

Rodgers, A., & Wahr, J. (1993, December). Inference of core-mantle boundary topography from ISC *PcP* and *PKP* traveltimes. *Geophysical Journal International*, *115*(3), 991–1011. doi: 10.1111/j.1365-246X.1993.tb01505.x

Schlaphorst, D., Thomas, C., Holme, R., & Abreu, R. (2016, February). Investigation of core–mantle boundary topography and lowermost mantle with P4KP waves. *Geophysical Journal International*, *204*(2), 1060–1071. doi: 10.1093/gji/ggv496

Sen, M. K., & Biswas, R. (2017, May). Transdimensional seismic inversion using the reversible jump Hamiltonian Monte Carlo algorithm. *Geophysics*, *82*(3), R119-R134. doi: 10.1190/geo2016-0010.1

Soldati, G., Boschi, L., & Forte, A. M. (2012, May). Tomography of core-mantle boundary and lowermost mantle coupled by geodynamics: Tomography of core-mantle boundary. *Geophysical Journal International*, *189*(2), 730–746. doi: 10.1111/j.1365-246X.2012.05413.x

Soldati, G., Boschi, L., Mora, S. D., & Forte, A. M. (2014). Tomography of core-mantle boundary and lowermost mantle coupled by geodynamics: Joint models of shear and compressional velocity. *Annals of Geophysics*, *57*(6), S0652. doi: 10.4401/ag-6603

Sze, E. K., & van der Hilst, R. D. (2003, January). Core mantle boundary topography from short period PcP, PKP, and PKKP data. *Physics of the Earth and Planetary Interiors*, *135*(1), 27–46. doi: 10.1016/S0031-9201(02)00204-2

Tanaka, S. (2010, April). Constraints on the core-mantle boundary topography from *P* 4 *KP-PcP* differential travel times. *Journal of Geophysical Research*, *115*(B4). doi: 10.1029/2009JB006563

Tarduno, J. A., Watkeys, M. K., Huffman, T. N., Cottrell, R. D., Blackman, E. G., Wendt, A., ... Wagner, C. L. (2015, July). Antiquity of the South Atlantic Anomaly and evidence for top-down control on the geodynamo. *Nature Communications*, *6*(1), 7865. doi: 10.1038/ncomms8865

Tkalčić, H., Romanowicz, B., & Houy, N. (2002, June). Constraints on D″ structure using PKP(AB-DF), PKP(BC-DF) and PcP-P traveltime data from broad-band records: Constraints on D″ structure. *Geophysical Journal International*, *149*(3), 599–616. doi: 10.1046/j.1365-246X.2002.01603.x

Tkalčić, H., Young, M., Muir, J., Davies, D., & Mattesini, M. (2015, December). Strong, Multi-Scale Heterogeneity in Earth's Lowermost Mantle. *Scientific Reports*, *5*, 18416.

Valentine, A. P., & Sambridge, M. (2018). Optimal regularisation for a class of linear inverse problem. , 35.

Vehtari, A., Gelman, A., & Gabry, J. (2017, September). Practical Bayesian model evaluation using leave-one-out cross-validation and WAIC. *Statistics and Computing*, *27*(5), 1413–1432. doi: 10.1007/s11222-016-9696-4

Yoshida, M. (2008, July). Core-mantle boundary topography estimated from numerical simulations of instantaneous mantle flow: CMB TOPOGRAPHY FROM NUMERICAL MODELS. *Geochemistry, Geophysics, Geosystems*, *9*(7), n/a-n/a. doi: 10.1029/2008GC002008

Young, M. K., Tkalčić, H., Bodin, T., & Sambridge, M. (2013, October). Global *P* wave tomography of Earth's lowermost mantle from partition modeling. *Journal of Geophysical Research: Solid Earth*, *118*(10), 5467–5486. doi: 10.1002/jgrb.50391

Supporting Information for "Long-wavelength topography and multi-scale velocity heterogeneites at the core-mantle boundary"

Jack B. Muir[1], Satoru Tanaka[2], Hrvoje Tkalčić[3]

[1]Department of Earth Sciences, University of Oxford,

South Parks Road, Oxford OX1 3AN, UK

[2]Volcanoes and Earth's Interior Research Center, Research Institute for Marine Geodynamics, Japan Agency for Marine-Earth Science and Technology,

2-15 Natsushima-Cho, Yokosuka 237-0061, Japan

[3]Research School of Earth Sciences, Australian National University,

142 Mills Road, Acton ACT 0200, Australia

Table S1. Table of hyperprior scales used to in the inversion.

Figure S1. Relative scale of the G kernel matrix elements shows the sensitivity of different degrees to different rays. Elements are plotted on a symmetric log scale, other than between ± 0.03 which is on a linear scale. The V_P and CMB radius kernels are separately normalized to the maximum amplitude value of $\boldsymbol{G}_{\delta s}$ and $\boldsymbol{G}_{\delta r}$, respectively. The vertical axis ticks show the edges of harmonic degree l, which are ordered from $m = -l$ to $m = l$ from bottom to top.

Figure S2. Travel time residuals for the 3 datasets used in this study. a) PcP-P, b) PKPab-PKPbc, c) P4KP-PcP Black histograms show the initial distribution of residuals, and green histograms show the deciles of remaining residual distributions after inversion.

Hyperprior scale	Value (Unit)
$\nu_{\delta r}$	5 (km)
$\nu_{\delta s}$	5 (s/Mm)
ν_{PcP-P}	2 (s)
$\nu_{PKPab-PKPbc}$	2 (s)
$\nu_{P4KP-PcP}$	2 (s)

Table S1. Table of hyperprior scales used to in the inversion.

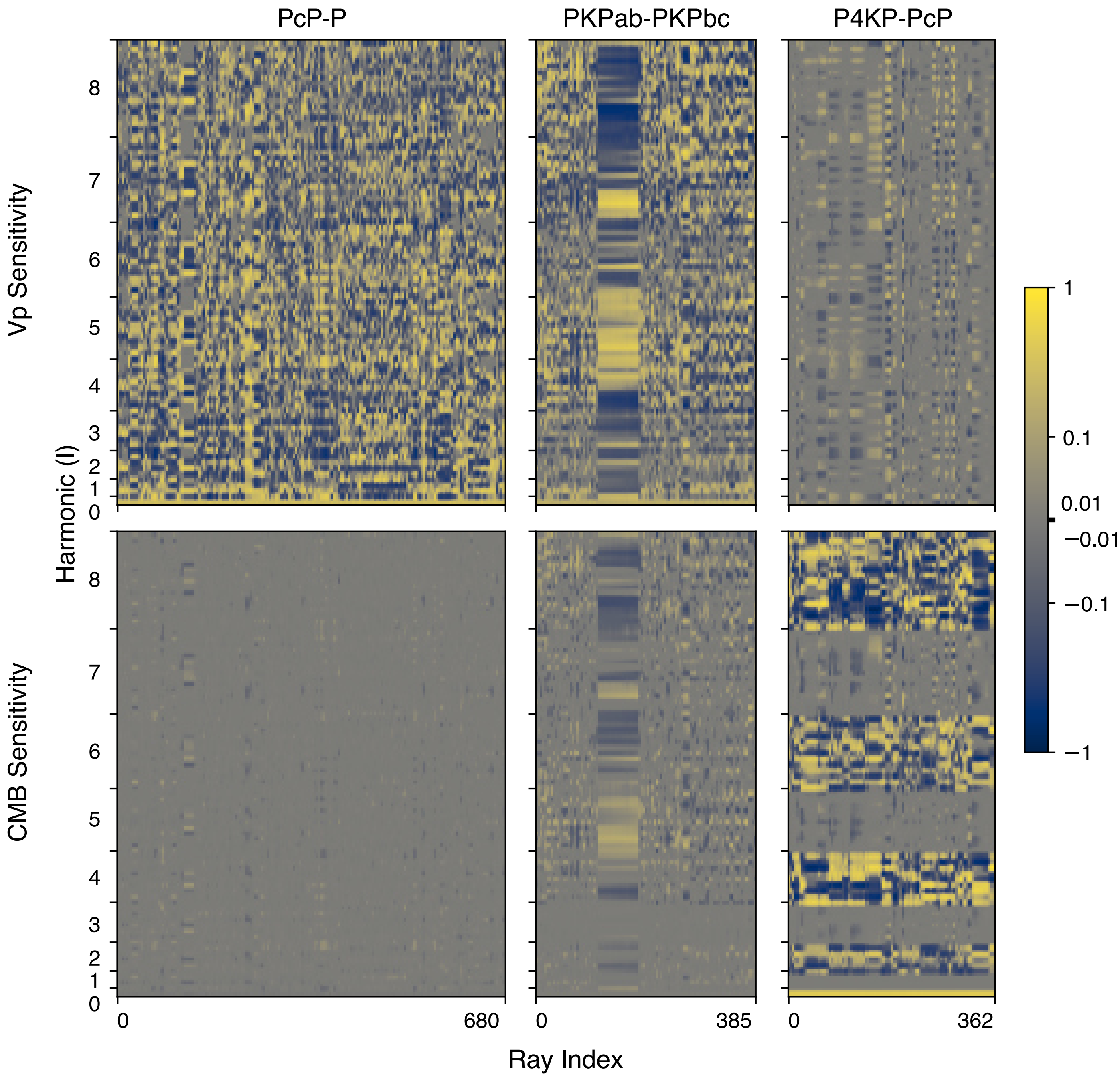

Figure S1. Relative scale of the G kernel matrix elements shows the sensitivity of different degrees to different rays. Elements are plotted on a symmetric log scale, other than between ± 0.03 which is on a linear scale. The V_P and CMB radius kernels are separately normalized to the maximum amplitude value of $\boldsymbol{G}_{\delta s}$ and $\boldsymbol{G}_{\delta r}$, respectively. The vertical axis ticks show the edges of harmonic degree l, which are ordered from $m = -l$ to $m = l$ from bottom to top.

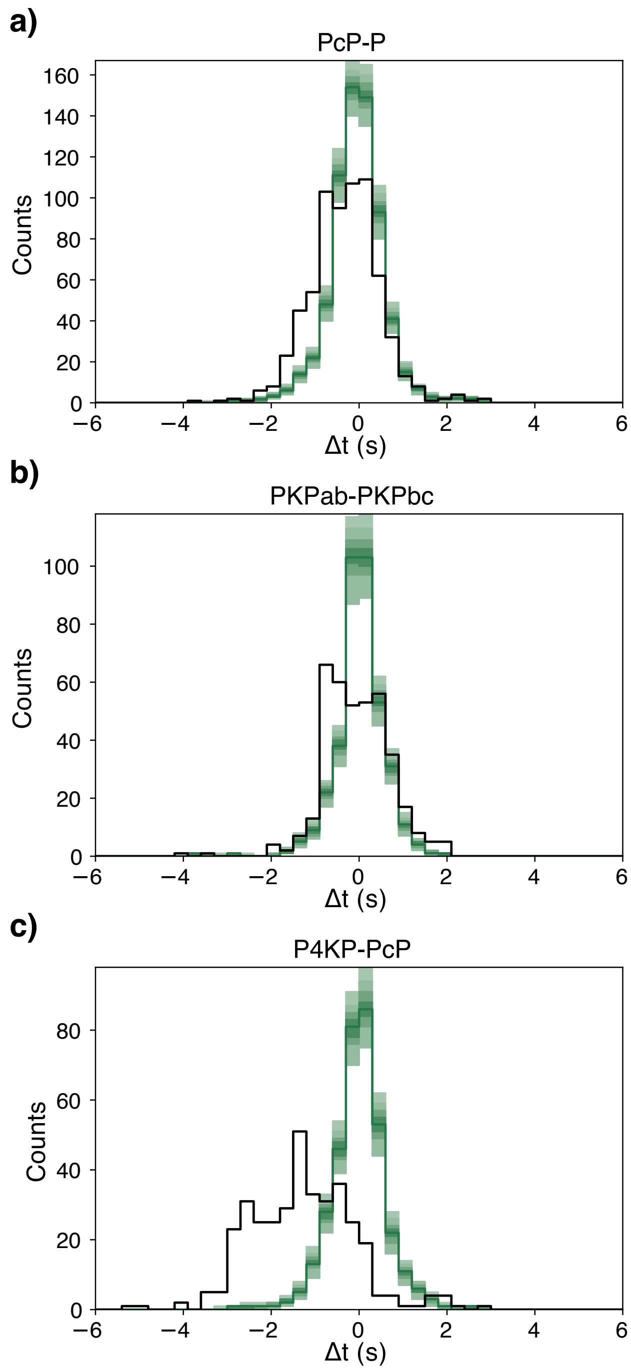

Figure S2. Travel time residuals for the 3 datasets used in this study. a) PcP-P, b) PKPab-PKPbc, c) P4KP-PcP Black histograms show the initial distribution of residuals, and green histograms show the deciles of remaining residual distributions after inversion.